ChemPubSoc Europe

DOI: 10.1002/chem.201902157

CHEMISTRY A European Journal Full Paper

Crystal Growth |*Hot Paper*|

Lattice Shrinkage by Incorporation of Recombinant Starmaker-Like Protein within Bioinspired Calcium Carbonate Crystals

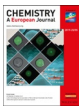

Mirosława Różycka,*[a] Ismael Coronado,[b] Katarzyna Brach,[c] Joanna Olesiak-Bańska,[c] Marek Samoć,[c] Mirosław Zarębski,[d] Jerzy Dobrucki,[d] Maciej Ptak,[e] Eva Weber,[f] Iryna Polishchuk,[f] Boaz Pokroy,[f] Jarosław Stolarski,[b] and Andrzej Ożyhar*[a]

Abstract: The biological mediation of mineral formation (biomineralization) is realized through diverse organic macromolecules that guide this process in a spatial and temporal manner. Although the role of these molecules in biomineralization is being gradually revealed, the molecular basis of their regulatory function is still poorly understood. In this study, the incorporation and distribution of the model intrinsically disordered starmaker-like (Stm-l) protein, which is active in fish otoliths biomineralization, within calcium carbonate crystals, is revealed. Stm-l promotes crystal nucleation and anisotropic tailoring of crystal morphology. Intracrystalline incorporation of Stm-l protein unexpectedly results in shrinkage (and not expansion, as commonly described in biomineral and bioinspired crystals) of the crystal lattice volume, which is described herein, for the first time, for bioinspired mineralization. A ring pattern was observed in crystals grown for 48 h; this was composed of a protein-enriched region flanked by protein-depleted regions. It can be explained as a result of the Ostwald-like ripening process and intrinsic properties of Stm-l, and bears some analogy to the daily growth layers of the otolith.

Introduction

Living organisms are capable of controlling mineral formation in a spatial and temporal manner. The biological control of mineralization (biomineralization) is undertaken by a complex set of macromolecules, proteins, in particular.[1] Proteins involved in biomineralization may have both a direct and indirect effect on depositing minerals.[2] The proteins that directly interact with the crystal structure include 1) insoluble matrix proteins (IMPs), which form a scaffold for the growing crystal and act as nucleators; and 2) soluble matrix proteins (SMPs), which control crystal size, shape, and polymorph selection.[1,3] SMPs are often highly negatively charged acidic proteins, which undergo extensive post-translational modifications, and frequently belong to the group of intrinsically disordered proteins (IDPs).[4–7] Additionally, proteins that act indirectly create the required conditions for the formation of mineral deposits. For example, certain classes of proteins are responsible for appropriate ion-concentration maintenance, some enzymes are involved in post-translational modifications, whereas other macromolecules may change the conformation of the nucleating proteins or organization of the mineralizing tissue.[2,8,9] The timing of protein synthesis and the activation and distribution pattern of proteins within the biogenic minerals (biominerals) are governed by molecular and cellular processes. As a consequence of the precisely structured incorporation of these proteins into the crystal structure, the physicochemical properties of biominerals are altered, in comparison to their synthetically or geologically formed counterparts.[10,11] Mollusk shells,[12] echinoderm ossicles,[13,14] vertebrate otoliths or otoconia,[15,16] and

[a] *M. Różycka, Prof. A. Ożyhar*
Department of Biochemistry, Faculty of Chemistry
Wroclaw University of Science and Technology, Wroclaw 50-370 (Poland)
E-mail: miroslawa.rozycka@pwr.edu.pl
andrzej.ozyhar@pwr.edu.pl

[b] *I. Coronado, J. Stolarski*
Institute of Paleobiology, Polish Academy of Sciences
Warsaw 00-818 (Poland)

[c] *K. Brach, J. Olesiak-Bańska, M. Samoć*
Advanced Materials Engineering and Modelling Group
Faculty of Chemistry, Wroclaw University of Science and Technology
Wroclaw 50-370 (Poland)

[d] *M. Zarębski, J. Dobrucki*
Department of Cell Biophysics, Faculty of Biochemistry
Biophysics and Biotechnology, Jagiellonian University
Krakow 30-387 (Poland)

[e] *M. Ptak*
Institute of Low Temperature and Structure Research
Polish Academy of Sciences, Wroclaw 50-422 (Poland)

[f] *E. Weber, Dr. I. Polishchuk, Dr. B. Pokroy*
Department of Materials Science and Engineering and
the Russell Berrie Nanotechnology Institute
Technion Israel Institute of Technology, Haifa 32000 (Israel)

Supporting information and the ORCID identification number(s) for the author(s) of this article can be found under: https://doi.org/10.1002/chem.201902157.

bones and teeth[2,17] are examples of biomineral skeletal elements, the structures of which are functionally modified by proteins and other organic macromolecules. Understanding the molecular basis of biomineralization can thus provide inspiration for the fabrication of new composite materials with strictly desired properties.

Fish otoliths, which are biomineral structures composed of inorganic calcium carbonate and an organic matrix that primarily consists of proteins and proteoglycans,[15] are formed extracellularly in the otolith organ of the inner ear and have two major roles in sensory functions. One, the vestibular sense, is related to the detection of linear accelerations produced by gravity and the other sense is hearing.[18] Otoliths are anchored to the sensory epithelium (or macula) containing hair cells. Changes in the position of the head of a fish or a sound cause the hair bundles to bend and subsequently depolarize the sensory hair cells. The emerging electrical signal is then relayed to the central nervous system.[15,19] Otolith formation is an acellular process. After initial seeding, the otolith is quickly attached to immature hair cells and rapidly grows during early ear development. Daily growth layers, which are subsequently added to the otolith during the life of the fish, vary in thickness and composition, depending on the circadian cycle and environment.[15,20–22] It has been shown that the calcium carbonate crystalline structure and the morphology of otoliths are regulated by an organic matrix.[23,24] Although the roles of matrix proteins in mineral formation are being gradually revealed, their time-dependent entrapping and distribution within the biomineral structure and molecular basis of their regulatory function is still poorly understood.

One of the fundamental areas of research into biomineralization is elucidating how organic macromolecules regulate mineral formation, their possible functions during crystal growth, and how they interact together.[25] The aim of this study is to analyze the distribution of intrinsically disordered SMPs in calcium carbonate crystals formed under controlled conditions in vitro by using starmaker-like (Stm-l) as the model protein. Stm-l from *Oryzias latipes* is a putative homolog of the starmaker (Stm) protein, which controls the shape and polymorph selection of the otolith in *Danio rerio*.[23,26,27] We have previously shown that Stm-l is a highly disordered protein able to adopt a more ordered and rigid structure.[28] An in vitro assay of the mineralization activity of Stm-l suggested that this protein affected calcium carbonate crystallization. Although Stm-l had a negative effect on the size of precipitating crystals, the higher number of crystals formed in the presence of the protein suggested that Stm-l could also act as a crystal nucleator.[28] This paper aims to elucidate interactions of the Stm-l protein and the mineral phase by studying the crystallographic properties of the resulting calcium carbonate crystals and by 3D visualization of the incorporation of the protein into the crystal lattice.

Results

In vitro $CaCO_3$ crystallization experiments

The crystalline phases of calcium carbonate identified in all experiments are calcite and vaterite; however, aragonite was also observed in the control sample. The regulatory control of the Stm-l protein in the morphology of the crystals varied according to the concentration of Stm-l. Calcite crystals grown in the absence of the protein are represented by a perfect rhombohedral morphology with the development of (104) and tautozonal faces (Figure 1 a, d). Calcite grown in a solution with 5 μg mL^{-1} of Stm-l developed a new family of (*hk*0) crystal faces, mostly the development of (110) and tautozonal faces parallel to the crystallographic *c* axis. The crystal size decreased and was shorter in the directions of the *a* and *b* axes and the newly formed faces were smooth (Figure 1 b, e). Crystals grown at a higher Stm-l concentration (i.e., 50 μg mL^{-1}) exhibited spherical to ellipsoidal morphologies, with smoothed edges and reduced expression of (104) and tautozonal faces. Crystals were shorter in the directions of all crystallographic axes with decreases in crystal size from approximately 58 to 32 μm after 48 h of growth (Figure 1 c, f). The protein displayed an inhibitory property in the development of (104) faces with increasing concentration (Figure 1 a–c).

On the other hand, vaterite spherical polycrystalline aggregates were formed in all experiments, including control experiments (data not shown). The crystal size remained essentially unchanged in all experiments, with differences in morphological variation. Vaterite crystals grown in the control experiment were spherical aggregates with sixfold symmetry formed by flaky crystal layers (about 3 μm in length and 300 nm wide) and a surrounding core depression. In the presence of Stm-l

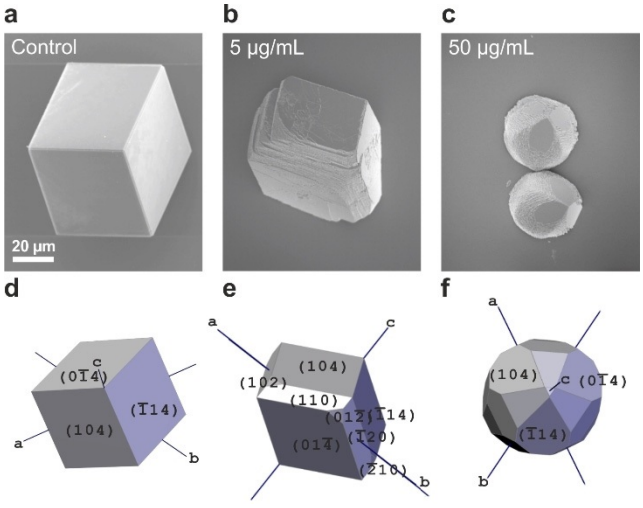

Figure 1. Morphological variations in the presence of Stm-l at different concentrations. SEM images of calcite crystals grown at different Stm-l concentrations (a–c) and their corresponding simulated theoretical 3D models (d–f), which were created by using the WinXMorph program.[57] Notably, the development of new faces, the decrease in size at different Stm-l concentrations, and the formation of ellipsoidal or spherical crystals can be observed. Crystals can be seen in all compositions of the (104) faces or other tautozonal planes.

(i.e., 50 μg mL^{-1}), completely spherical vaterite crystals were formed with framboidal morphology, without depressions, and composed of layered granules of approximately 9 μm.

Incorporation of Stm-I into the crystal lattice of calcium carbonate crystals

The function of the protein as a crystallization–nucleating agent may be associated with its particular localization in the growing crystal. We performed high-resolution X-ray powder diffraction (HRPXRD) analysis to determine whether Stm-I was incorporated into the lattice of calcium carbonate crystals and how this affected the microstructure of the host crystals (crystallite size and microstrain), which could have been related to the interplay of the protein with the mineral phase. XRD data revealed a shift in the positions of the diffraction peaks of the Stm-1/calcite crystals toward higher 2θ angles, compared with those of the control experiments, which implied that the Stm-I protein indeed became incorporated within the calcite lattice. Figure 2a shows a shift in the (104) reflection, which was higher at a Stm-I concentration of 50 μg mL^{-1} than that of 5 μg mL^{-1}. In the absence of protein, the unit cell parameters of synthetic calcite were $a=b=4.991194(7)$ Å and $c=17.06189(3)$ Å. Addition of the Stm-I protein at concentrations of 5 and 50 μg mL^{-1} caused a change in lattice parameters to $a=b=4.991051(7)$ Å and $c=17.06267(3)$ Å, and $a=b=4.989144(10)$ Å and $c=17.05540(5)$ Å, respectively (see Table S1 in the Supporting Information). The obtained results revealed negative shrinkage-like lattice distortions in the presence of Stm-I, with an evident reduction in lattice volume (Table S1 in the Supporting Information). The strain calculated in synthetic calcite with regards to the control sample[29,30] for the highest Stm-I concentration was $\Delta a/a=-4.1\times10^{-4}$, $\Delta c/c=-3.8\times10^{-4}$, and $\Delta V/V=-1.2\times10^{-3}$ (Figure 2f). The use of HRPXRD allowed us to determine the crystallite size and average microstrain fluctuations for each sample. Figure 2g shows the results of calculating the crystallite size by using the methods of Caglioti and Scherrer[31,32] (see Table S2 in the Supporting Information); this was significantly reduced for both protein concentrations: 320–426 and 324–485 nm for 5 and 50 μg mL^{-1} Stm-I, respec-

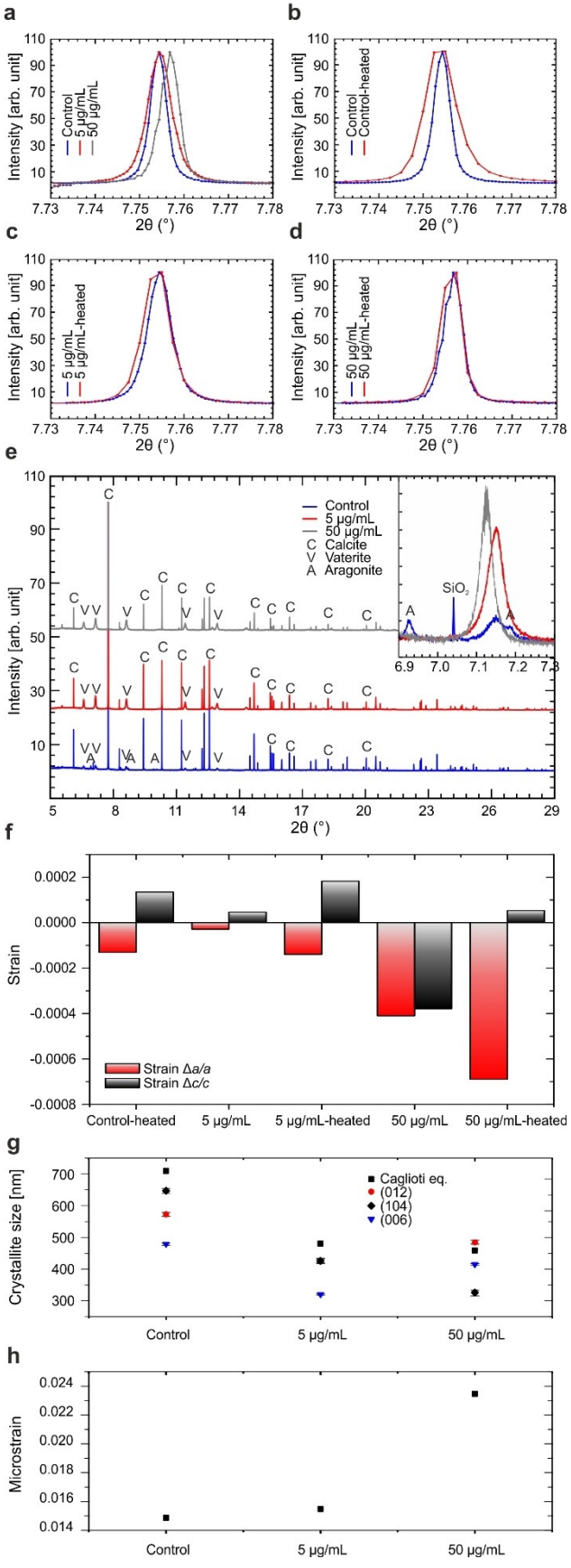

Figure 2. Incorporation of Stm-I into the crystalline lattice of synthetic calcium carbonate. a)–d) The (104) XRD reflection of crystals of synthetic calcite. The presence of intracrystalline Stm-I caused a shift in the XRD reflections, which was highest for a Stm-I concentration of 50 μg mL^{-1}. Heat treatment was accompanied by a broadening of the diffraction peak, which was greater in the control sample. e) Crystalline phases of calcite and vaterite were identified in each experiment. The inset shows a shift in the (101) reflection of crystals of synthetic vaterite at a Stm-I concentration of 50 μg mL^{-1} (some reflections of aragonite in the control sample are also included). f) Strain calculations of synthetic calcite with regard to the control sample. The most prominent lattice distortions occurred along the *c* axis and were higher at a concentration of 50 μg mL^{-1}. Relaxation of the lattice after heat treatment was accompanied by an increment of strain in $\Delta a/a$ and $\Delta c/c$ in all the samples. g) Calculations of crystallite size for the synthetic crystal calcite. The Caglioti and Scherrer equations showed a strongly reduced crystallite size with increases in the Stm-I concentration. The decrease in crystallite size calculated in the (104) plane with a Stm-I concentration of 5 μg mL^{-1} was greater than that with 50 μg mL^{-1}, for which a larger decrease occurred in the (006) plane. h) Microstrain fluctuations calculated for synthetic crystal calcite. The microstrain fluctuations increased with decreases in crystallite size.

tively, with regard to the control calcite (478–647 nm). Decreases in the crystallite size calculated in the (104) plane with a Stm-l concentration of 5 μg mL^{-1} was greater than that for a Stm-l concentration of 50 μg mL^{-1}, with larger decreases in the (006) plane (Table S3 in the Supporting Information). The calculated microstrain fluctuations increase with reduced crystallite size (Figure 2h). Owing to the presence of Stm-l in the calcite crystals, microstrain fluctuations increased from 0.0149 to 0.0155% for a concentration of 5 μg mL^{-1} and increased to 0.240% with 50 μg mL^{-1} of Stm-l.

Ex situ heat treatment was accompanied by a broadening of the diffraction peaks and this also increased in the control sample. In pure calcite crystals, such broadening of the diffraction peaks should not be expected; however, all samples, including the control, were grown in the presence of TRIS buffer and most likely the incorporation of TRIS compounds into the lattice could explain observed broadening of diffraction peaks for the control (Figure 2b). In all samples, including the control, after heat treatment, the lattice volume decreased. This can be explained by relaxation of the negative strain along the *c* axis combined with even bigger contraction along the *a* axis due to relaxation along the *c* axis. These results were more prominent as the protein concentration increased. Our results indicated that Stm-l interacted distinctly with the mineral phase, depending on the Stm-l concentration.

Distribution of Stm-l in calcium carbonate crystals

Two-photon microscopy (TPM) was used to elucidate the distribution of AF488-labeled Stm-l (Stm-l/AF488) in synthetic calcite. The collected data indicated that Stm-l was located inside the crystal, in particular, in the central part (Figure S1 in the Supporting Information). However, TPM does not provide an improvement in spatial resolution over that achieved through confocal laser scanning microscopy (CLSM) and in some circumstances the use of confocal microscopy may be more advantageous.[33] Thus, CLSM was the next tool used for a more precise determination of the localization of Stm-l in calcite crystals. Figure 3 shows confocal laser scanning micrographs stacked in the *z* direction of calcium carbonate precipitated

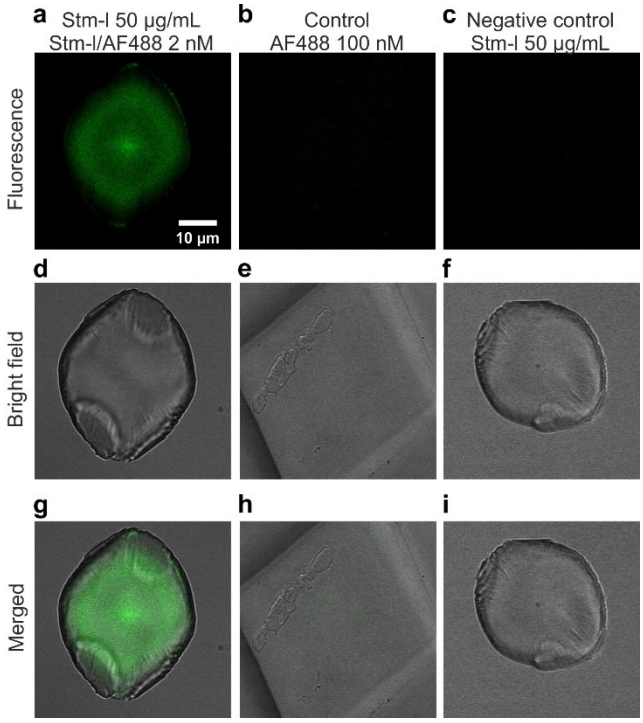

Figure 3. Confocal laser scanning images of calcium carbonate crystals. Confocal images stacked in the *z* direction of representative crystals grown in the presence of Stm-l with a total concentration of 50 μg mL^{-1}, including Stm-l/AF488 with a concentration of 2 nM (a, d, g), in the presence of AF488 with a concentration of 100 nM (b, e, h), and in the presence of Stm-l with a concentration of 50 μg mL^{-1} (c, f, i). a–c) The fluorescence distribution within the crystalline structures. d, f) Bright-field images of representative crystals. g–i) Merged bright-field and fluorescent images. Concentrations of calcium ions were 10 mM. The time for crystal growth was 48 h. Scale bar: 10 μm.

with different additives. We did not observe fluorescence in the control group of crystals precipitated with AF488 dye or in the presence of unlabeled Stm-l (Figure 3b, e, h, and c, f, i, respectively). CLSM performed in the presence of Stm-l/AF488 made it possible to reveal the distribution of protein in calcite crystals growing in vitro (Figure 3a, d, g). Specifically, fluorescence was distributed concentrically and was intense mainly at the center of the particle (Figure 4). Moving from the center of

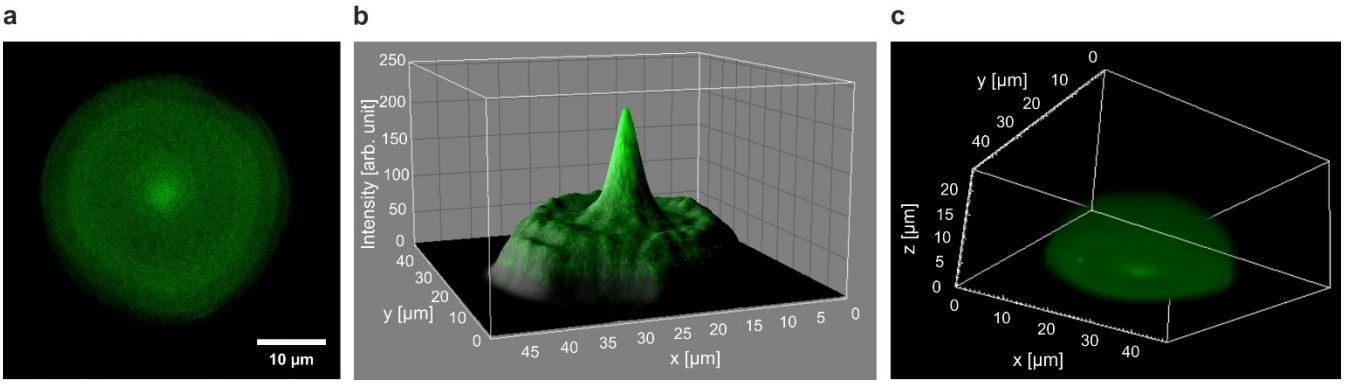

Figure 4. Ring pattern distribution of Stm-l in calcium carbonate crystals. a) Confocal image stacked in the *z* direction of the representative crystal grown in the presence of Stm-l at a total concentration of 50 μg mL^{-1}, including Stm-l/AF488 with a concentration of 2 nM. The concentration of calcium ions was 10 mM. The time for crystal growth was 48 h. Scale bar: 10 μm. b) Quantitative analysis of the fluorescence intensity distribution of the CLSM micrograph in a). c) 3D confocal image stacked in the *z* direction of the crystal present in a) and b).

the crystal along its radius, fluorescence decreased, then slightly increased to form a ring around the center, and again decreased near the edge of the crystal. It is worth noting that the fluorescence intensity of the ring was not as good as that in the central part of the crystal (Figure 4b). The 3D projection shown in Figure 4c was performed by using *z*-stacked images of a representative calcite crystal (118 *z* positions, with an interval of 0.21 μm), excluding the possibility of misinterpretation caused by a biased choice of the *z* position present in Figure 4a and b. Interestingly, Stm-l/AF488 was also weakly visible in vaterite, especially in the central part (Figure S2 in the Supporting Information). However, the amount of protein in vaterite was much smaller than that in calcite. These results clearly show the heterogeneous distribution of Stm-l in the formation of calcite crystals. This characteristic localization may be the result of the intrinsic properties of the Stm-l protein, which directs the modulation of crystal growth.

Time-dependent mineralization experiments

In addition, time-dependent crystallization tests were performed to examine the morphology of growing crystals and possible changes in the distribution of Stm-l during crystal formation. In these experiments, calcium carbonate crystal growth was stopped after 2, 4, 6, 8, 10, 12, 16, 20, 24, 36, or 48 h and a Stm-l concentration of 50 μg mL^{-1} was used for each experiment. SEM observations indicated that, after 6–8 h of crystal growth, small, smooth, and rounded crystals had formed (Figure 5a, b, g, h). Interestingly, during this time, additional smaller crystals sticking to the edge of the biggest one were visible. However, they disappeared after a longer mineralization time. After 10 h of the assay, the crystals noticeably showed rounded edges and characteristic stairlike structures (Figure 5c–f, i–l).[28] It is worth noting that, when crystals were forming, growth was rather moderate during up to 20 h and then a significant increase in crystal diameter was observed (Figure 6).

In parallel, CLSM was used to analyze the distribution of Stm-l in the obtained crystals (Figure 7). All crystals shown in Figure 7 are calcite (Figure S3 in the Supporting Information); however, the formation of vaterite crystals can also be seen (as reported previously[28]). Nevertheless, we focused our analysis on calcite crystals because of the very weak incorporation of Stm-l into the vaterite crystals. Unexpectedly, CLSM imaging showed that, although there were no observable crystals under SEM after 2 and 4 h of crystal growth, small fluorescence spots were then noticeable (Figure 7a, b, i, j, q, r). Smooth crystals formed after 6–8 h of mineralization showed intense fluorescence in the center of the particles, whereas smaller crystals that were stuck to the edge of the biggest one had no fluorescence in the inner part (Figure 7c, d, k, l, s, t). After 10 h of mineralization, the fluorescence ring appeared close to the edges, yet the crystals were still significantly smaller than those obtained after 48 h (Figure 7e, f, m, n, u, v). After 24 h of mineralization, the ring pattern appeared to be fully formed (Figure 7g, h, o, p, w, y). These tests made it possible to visualize the sequential deposition of Stm-l within the formed calcite crystals. First, protein molecules involved in the nucleation of a crystal were entrapped in the central part of the mineral particle. Then, Stm-l was anisotropically deposited, tailoring the crystal morphology, and it was successively entrapped within the enlarging calcite crystals that developed at the expense of the smaller crystals, which dissolved.

Discussion

The remarkable physical properties of biogenic minerals, in comparison to geological and synthetic counterparts,[34] are largely related to the presence of an inter- and/or intracrystalline organic phase, which constitutes only a few percent of the total weight of the biomineral. For example, the intercrystalline organic macromolecules in mollusk shells[35] that wrap up individual crystallites, facilitate crack arrest and deflection at interfaces between organic and inorganic phases.[36] The possible functional role of intracrystalline macromolecules, such as Stm-l, is still poorly understood.[29,35,37,38] Our previous biochemical characterization of Stm-l suggested that the extended and pliable conformation of this protein might facilitate its interaction

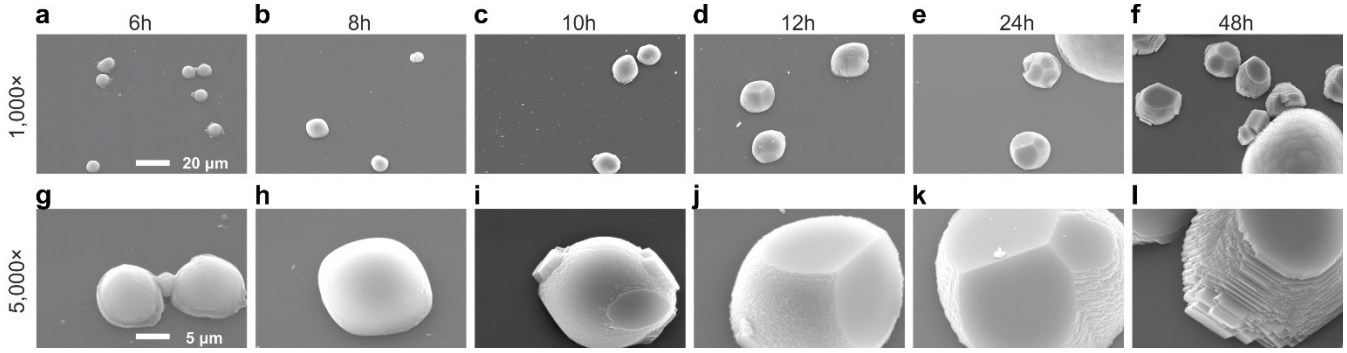

Figure 5. SEM images of crystals obtained at different times of crystallization in the presence of Stm-l/AF488. SEM images of representative crystals grown in the presence of Stm-l with a total concentration of 50 μg mL^{-1}, including Stm-l/AF488 with a concentration of 2 nM at different times of growth. The in vitro crystallization experiments were stopped after 6 (a, g), 8 (b, h), 10 (c, i), 12 (d, j), 24 (e, k), and 48 h (r, l). a–f) 1000× magnification of representative crystals. g–l) 5000× magnification of the same crystals as those shown in a–f). The concentration of calcium ions was 10 mM. Scale bar in a): 20 μm; scale bar in g): 5 μm.

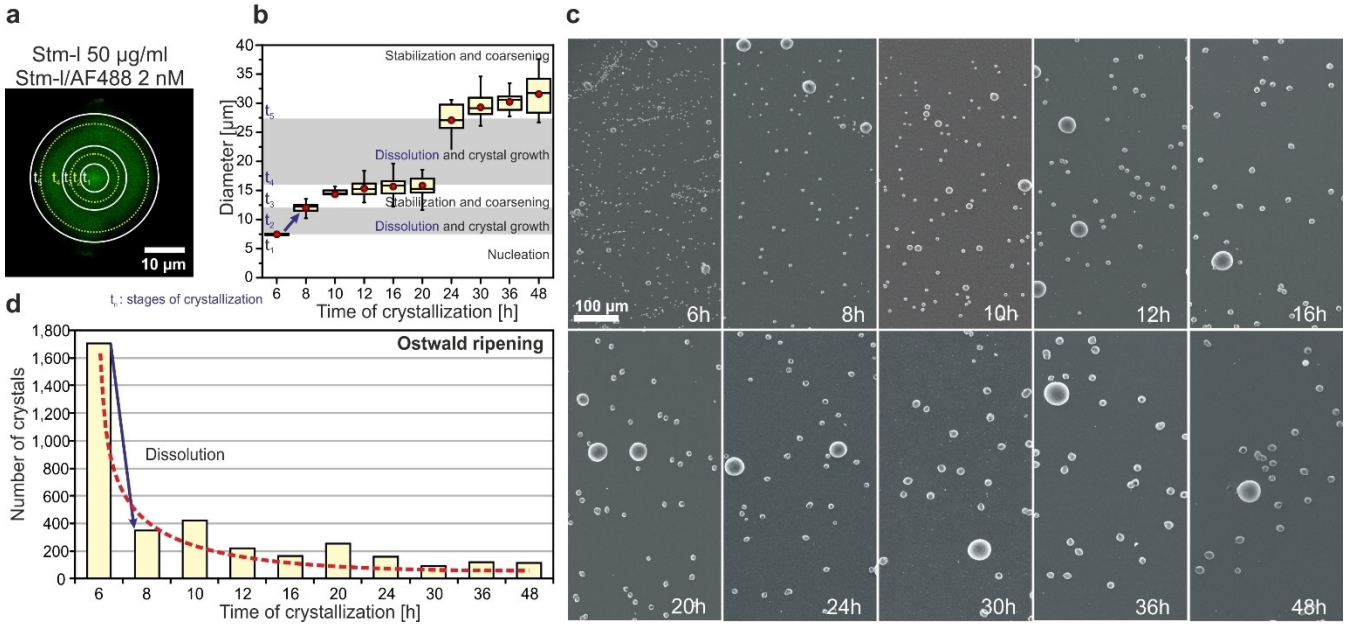

Figure 6. Ostwald ripening of $CaCO_3$ crystals with Stm-l at a total concentration of 50 µg mL^{-1}, including Stm-l/AF488 with a concentration of 2 nM at different times. a) Confocal images stacked in the *z* direction of a representative crystal (Figure 3 a) grown for 48 h. t_n are the settings of the main stages of crystallization indicated by the mean diameter of box charts and circles represent the mean diameter of such limits. b) The box chart presents the measured distribution of diameters per crystal group obtained at different time points. The horizontal line and red dot within the box represent the median and mean of the distributions, respectively. c) SEM images of crystals obtained at different times of crystallization, showing differences in crystal concentration and size. d) Bar plot showing the number of crystals calculated at different times. The red line shows the asymptotic decrease in the number of crystals over time.

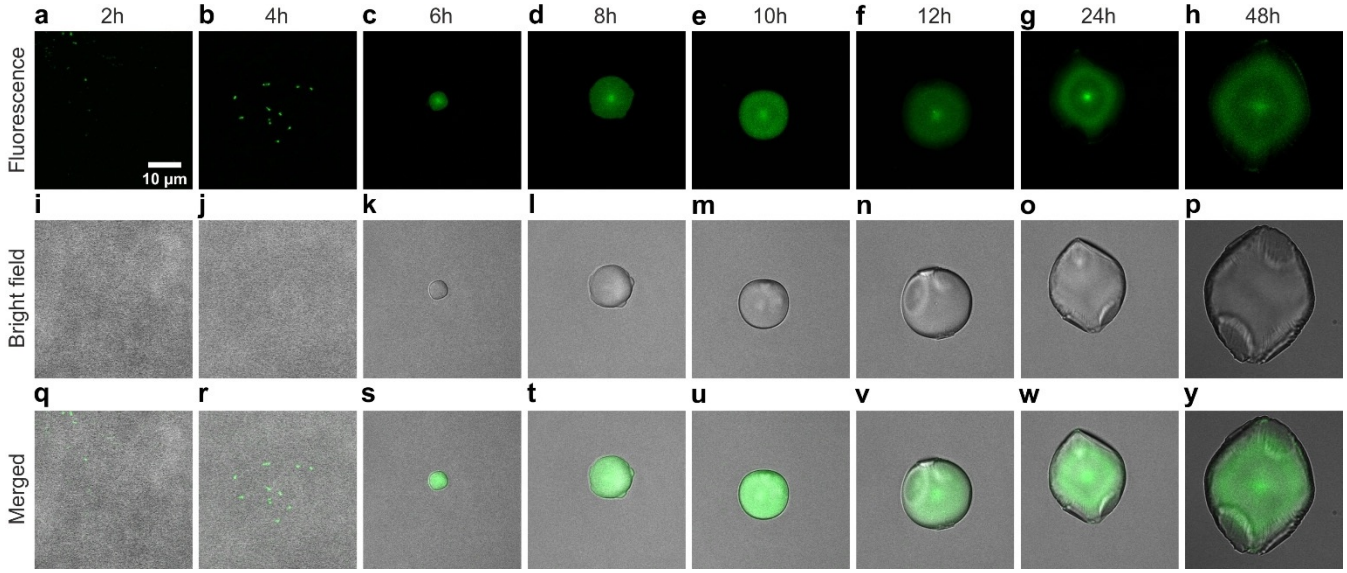

Figure 7. Confocal laser scanning micrographs of crystals obtained at different times of crystallization in the presence of Stm-l/AF488. Confocal images stacked in the *z* direction of representative crystals grown in the presence of Stm-l with a total concentration of 50 µg mL^{-1}, including Stm-l/AF488 with a concentration of 2 nM at different times of growth. The in vitro crystallization tests were stopped after 2 (a, i, q), 4 (b, j, r), 6 (c, k, s), 8 (d, l, t), 10 (e, m, u), 12 (f, n, v), 24 (g, o, w), and 48 h (h, p, y). a–h) Fluorescence distribution within the crystalline structures. i–p) Bright-field images of representative crystals. q–y) Merged bright-field and fluorescent images. The concentration of calcium ions was 10 mM. Scale bars: 10 µm.

with inorganic constituents of biominerals and other proteins in the organic matrix of otoliths. This was supported by the influence of Stm-l on the morphology (formation of ellipsoidal–spherical crystals of reduced size) and on the number of calcium carbonate crystals obtained in vitro.[28] Herein, we tried to elucidate how the protein was incorporated into the calcite crystals. The HRPXRD results revealed that the presence of Stm-l caused a shift in reflections to higher Bragg angles (smaller *d* spacing), which was more prominent at a Stm-l concentration of 50 µg mL^{-1}. The lattice parameters calculated, relative to the control crystals obtained without the protein, indicated that Stm-l at a concentration of 50 µg mL^{-1} caused nega-

tive (shrinkage-like) distortions in both the *a* and *c* axes (lattice volume reduction). In addition, the crystallite size was significantly reduced, even at a very small concentration of Stm-l, and microstrain fluctuations increased. Lattice distortions caused by Stm-l are similar to those produced by Mg^{2+} in the calcite crystal lattice.[35,39] The isomorphic replacement of Ca^{2+} by Mg^{2+} reduced the lattice volume almost proportionally to the Mg^{2+} concentration,[35] because the ionic radius of Mg^{2+} is almost three times shorter than Ca^{2+} (72 and 197 pm, respectively). This suggests that the position of Stm-l within the crystal or its interaction with the mineral phase may cause similar lattice shrinkage proportionally to the concentration of Stm-l. Interestingly, the incorporation of free amino acids into the calcite host lattice induced positive distortions in the *c* axis.[40]

Annealing experiments provided additional insights into organic macromolecule properties and their interactions with the mineral phase. Under annealing of biominerals (e.g., mollusk shells[41]) and some bioinspired materials,[42] intracrystalline macromolecules may break down into small pieces, resulting in strain relaxation. It has been suggested that, after thermal decomposition, fragments of macromolecules become chaotically distributed within the crystal, causing a reduction in the size of the crystalline blocks and increasing microstrain fluctuations.[43] As a result, XRD peak profiles were considerably broader.[41] In contrast, our XRD measurements after heating showed that the lattice volume was partially contracted, resulting in the observation of a small decrease in coherence length. We have noted previously,[28] however, that the Stm-l protein is very stable at high temperatures. The protein heated at 80 °C, after renaturation, returned to its original structure.

Circular dichroism (CD) spectra of Stm-l indicated that the protein adopted a more ordered and rigid structure with increasing temperatures.[28] This response to heat is another characteristic feature of IDPs,[44] to which Stm-l belongs.[28] Increasing the secondary-structure content probably leads to a reduction in the size of the molecule. These results could explain the higher negative $\Delta V/V$ distortion after heating the sample grown at a concentration of 50 $\mu g\,mL^{-1}$ Stm-l protein; this was most prominent in $\Delta a/a$. Our results showed that Stm-l had a tendency to adhere to certain crystallographic planes (Table S3 in the Supporting Information).

Crystallite size increased substantially at the (104) and (006) planes in the ex situ heated sample. With compaction of the molecule, these interactions changed and showed even stronger distortions (i.e., shrinkage) along the *a* and *b* axes, whereas strain along the *c* axis was lessened. Additionally, our data showed that the protein was located inside the crystals; thus the thermal resistance of Stm-l may additionally be enhanced by this location. The thermal resistance of the Stm-l protein is consistent with our current experimental data. After heating at 250 °C, a significant broadening of the XRD reflection peaks, with a simultaneous decrease in crystallite size, was observed only in the control samples grown in the presence of TRIS buffer, but without the protein. The parameters of crystals with the Stm-l protein changed to only a very small extent. Annealing of calcite with Stm-l at a concentration of 50 $\mu g\,mL^{-1}$ resulted in a higher negative $\Delta a/a$ distortion than that of the nonheated sample, and the lattice volume was strongly reduced. This anisotropic behavior of bioinspired crystals after annealing, that is, contraction of the *a* axis (lattice volume decrease), resembles annealing of the coccolith calcite of *Emiliana huxleyi*.[43] In contrast, Stm-l has been shown to differ significantly in thermal behavior to that of another recombinant protein from *Haliotis laevigata*, perlucin.[30] Annealing at 250 °C was sufficient to damage the recombinant green fluorescent protein (GFP) perlucin in the calcite.[30] Perlucin is involved in mollusk shell biomineralization and, as a member of the lectin protein family,[45] is more ordered than that of Stm-l. Thus, it could interact with calcite in a completely different manner to that of Stm-l. It should be noted that the obtained HRPXRD results are averaged values for the whole volume of the crystal. The protein could be distributed heterogeneously inside the crystal, which would cause local lattice distortions. In fact, the TPM and CLSM experiments performed revealed that Stm-l had a very specific localization in the calcium carbonate crystals obtained in vitro. Both techniques clearly and unambiguously showed the presence of protein-poor and -rich regions within the obtained crystals. Thus, the effect observed in HRPXRD is an average of different effects caused by Stm-l inside growing crystals.

In our previous study involving crystallization experiments, we observed the formation of two polymorphs of calcium carbonate, calcite and vaterite, which were also present in the control experiment without the protein.[28] In this study, AF488-labeled Stm-l (Stm-l/AF488) was visible in the central part of both polymorphs; however, the amount of Stm-l in vaterite was much smaller than that in calcite. This observation is consistent with our previous hypothesis that Stm-l acts as a nucleator of crystal growth, probably because of the high content of charged amino acid residues in the Stm-l sequence, which could cause calcium and carbonate ions from the solution to gather and promote crystal nucleation. Herein, we note that the occurrence of the protein in vaterite is probably only limited to its nucleation site, whereas in calcite the distribution of Stm-l occurs throughout almost the entire crystal; thus suggesting that, despite the fact that Stm-l does not control polymorph selection, it has a much higher affinity to the calcite form. One may speculate that the affinity of Stm-l to calcite is rooted in the specific spatial organization of the crystal lattice and/or a specific lattice volume requirement. In this regard, the lattice volume of the hexagonal symmetry of vaterite ($P6_3/mmc$, in this study) was almost three times smaller than the trigonal symmetry ($R\bar{3}c$) of calcite. Unlike other crystallization experiments in the presence of recombinant proteins, such as that reported by Weber et al.,[30] in which proteins were located in specific areas in the crystals and represented the mineral texture, crystals grown in the presence of Stm-l form a characteristic ring pattern (zonation) distribution. These remarkable rings, the pattern of which resemble that of geological Liesegang rings, are composed of a protein-enriched region flanked by protein-depleted regions. Their formation is explained herein by the Ostwald-like ripening process,[46,47] in which $CaCO_3$ crystals grow by pulses or stages (Figure 6). This interpretation is consistent with data provided by time-dependent

crystallization experiments in the analysis of the localization of Stm-l, the number of crystals formed over time, and the diameter of the crystals. First, we observed the gathering of protein molecules and ions as small fluorescent spots by using CLSM. These dynamic formations are probably too unstable to visualize small nuclei under SEM. This observation suggests the presence of dense liquid droplets (intermediate phases) at the early stages of calcium carbonate crystallization in the presence of Stm-l, according to the prenucleation cluster (also known as nonclassical) pathway proposed by Gebauer and coworkers,[48,49] and is consistent with the interpretation that this protein acts as a nucleator during calcium carbonate formation. After 6 h (t_1; Figure 6), thousands of small, smooth, and rounded crystals were formed, and, in contrast with the hundreds formed in the control experiment, the fluorescence at this time was concentrated at the center of the particles. After 8 h of the experiment (t_2), the crystal size increased and the number of crystals decreased substantially (4 times less). This new stage of growth (almost doubled in size), followed by a partial dissolution of a smaller fraction of crystals, released the Stm-l protein in solution, which was newly incorporated in the newly formed area, exhibiting a rather more uniform distribution of the protein. At this time point, additional smaller crystals were visible sticking to the edge of the biggest one (t_3). They were characterized by an even distribution of Stm-l and were visible for only a short period, disappearing after the next 2 h of mineralization. From this time (t_4, after 20 h), calcite crystals grew slowly and stabilized in the next 10 h and, interestingly, a protein-rich structure started to appear in the form of a ring. A fraction of the calcite crystal dissolved, reducing the population by 1.6 times, whereas large crystals grew quickly. The crystal population stabilized in the second 24 h period, showing slow crystal growth and, after the second stage of ripening, coarsening with a depletion of the protein. It should be highlighted that dissolution continued, along with maturation of the crystals, and the population decreased. Consistently with the Ostwald ripening process, variations in the supersaturation state of a solution create a diffusion gradient at which small crystals are dissolved, together with the release of embedded Stm-l protein. Released Stm-l, together with inorganic ions, follows a diffusion gradient towards larger growing crystals, which are thermodynamically preferred.[50] The crystal size distribution of some box charts are similar to those of the biased population of crystals grown by the Ostwald ripening described previously,[51] for example, at 8, 20, and 24 h. Repetition of this process, most likely due to fluctuations in the supersaturation state, resulted in several Stm-l-enriched rings observed within the larger crystals, with the dissolution of previous crystal clusters (the population was asymptotically reduced about 15 times from 6 to 48 h). Notably, the Stm-l protein is present in protein-poor regions at a lower concentration; this excludes the possibility that the ring pattern formation was caused by the complete depletion of Stm-l in solution and confirmed the biomineralization role of this protein. Moreover, Stm-l was not significantly incorporated into the vaterite crystals, especially in the central part, and some morphological variations were observed, probably for this reason. The lattice volume did not vary significantly. Różycka et al. reported that after 336 h (2 weeks) vaterite was also completely dissolved.[28] This means that the Ostwald ripening process continues at the expense of dissolution of vaterite, even if the crystals are larger than that of calcite. However, the participation of the protein to control this process is evident, especially in the stabilization of crystals at particular stages at which crystal growth slows down considerably. In contrast to the commonly described expansion of the unit cell in biogenic calcites, the observed shrinkage of the volume of calcite crystals upon interaction with Stm-l (proportional to the protein concentration), together with localization of the protein in crystals indicates a unique location of the Stm-l protein within the calcite crystal lattice or hypothetically different behavior (thus location) in the nonnative mineral lattice (calcite vs. aragonite native crystals for otoliths). It should be noted that the time-dependent alternating organic/inorganic layers are one of the most important attributes of fish otoliths. Although native Stm-l could interact differently with the aragonitic crystal lattice, we believe that the knowledge gained on the distribution of Stm-l in calcitic crystals and the properties of the protein molecules determined may have direct implications for understanding the role of proteins in otolith biomineralization. For example, the diurnal pattern of deposits and the slight dissolution of some fraction of the calcium carbonate deposits of fish otoliths may result in similar patterning of protein-enriched phases that are observed in our in vitro experiments. Importantly, the active behavior of the Stm-l protein in calcium carbonate mineralization may provide the potential to open up promising strategies for designing new biomimetic materials with remarkable and strictly desired properties.

Conclusions

Although, over the last few decades, the ability to identify an often large number of macromolecules involved in biomineralization has grown and expanded, major questions on specifically how these macromolecules interact with the mineral phase still remain open. The results of this study are relevant to understand the functional significance of the Stm-l protein in calcium carbonate mineralization. HRPXRD results indicated that recombinant Stm-l was incorporated into the calcite crystallite, which caused shrinkage of the crystal lattice. It is interesting to note that, to the best of our knowledge, this is the first time that such an effect has been described as being caused by an intracrystalline macromolecule within synthetic calcite crystals. The incorporation of Stm-l into the calcite crystal caused anisotropic tailoring of the crystal morphology, depending on the protein concentration used. CLSM analysis revealed that the protein was concentrated at the center of the particle and then formed rings around the center composed of a protein-rich region flanked by protein-poor regions. The time-dependent mineralization tests made it possible to visualize the sequential deposition of Stm-l in forming calcite. We found that the protein acted as a nucleator of crystal growth through the condensation and formation of intermediate phases at the early stages of the process. Then, Stm-l regulated crystal

growth by adhering to step edges on calcite, which resulted in ellipsoidal to spherical shapes of crystals and a reduction in crystal/crystallite sizes. The Ostwald ripening process explains the several Stm-l-enriched rings observed within the larger crystals. Numerous small crystals observed at the beginning of crystallization dissolved, together with the release of embedded Stm-l protein, which subsequently, together with inorganic ions, contributed to the formation of larger crystals. Repetition of this process, most likely due to fluctuations in the supersaturation state, resulted in a ring pattern. To the best of our knowledge, this is the first report on the time-dependent distribution of a single protein in crystals obtained in vitro. This is also the first time that the effect of a protein involved in the formation of otoliths on the calcium carbonate crystal lattice has been studied.

Experimental Section

Buffers

All buffers were prepared at 24 °C. Buffer A was 20 mM TRIS, 150 mM NaCl, pH 7.5. Buffer C was 100 mM $NaHCO_3$, 150 mM NaCl, pH 8.3. All reagents were obtained from Carl Roth GmbH + Co. Kg, Karlsruhe, Germany.

Protein preparation

Recombinant, nontagged Stm-l protein was obtained as previously described.[28] Briefly, Stm-l was overexpressed in BL21(DE3)pLysS *Escherichia coli* cells (Merck KGaA, Darmstadt, Germany) and purified through fractionation with ammonium sulfate, size-exclusion chromatography, and anion-exchange chromatography. The obtained protein was desalted to buffer A and stored at −80 °C. The protein concentration was determined spectrophotometrically at $\lambda = 280$ nm.

Protein labeling

For fluorescence labeling of Stm-l, buffer A was changed to buffer C by using the Amicon Ultracel 2 mL centrifugal filter with a cutoff limit of 10 kDa. Protein in buffer C was incubated with a tenfold molar excess of Alexa Fluor 488 NHS ester dye (AF488, Thermo Fisher Scientific, Waltham, MA, USA; dissolved in DMSO) for 1.5 h at 24 °C in the dark. Unreacted AF488 was removed by means of size-exclusion chromatography by using a Superdex 200 10/300 GL column connected to the ÄKTAexplorer system (GE Healthcare, Boston, Massachusetts, USA). The labeled protein (Stm-l/AF488) concentration and the degree of labeling (DOL) were determined spectrophotometrically by measuring the absorbances at $\lambda = 280$ and 494 nm. The calculated DOL was 1.9.

In vitro $CaCO_3$ crystallization experiments

Calcium carbonate mineralization was performed according to a previously described protocol,[28] with the following slight modifications:

For two-photon fluorescence microscopy, 96-well microplates for the cellular culture containing a round glass coverslip in each well were used. Into each well, solution (200 μL) was added that contained 10 mM $CaCl_2$ and a total protein concentration of 50 μg mL^{-1}, including labeled Stm-l/AF488 with a concentration of 10 nM, unlabeled Stm-l with a concentration of 50 μg mL^{-1} (for the negative control), or 100 nM AF488 (for the control experiment). The time of growth was 48 h.

For CLSM and SEM, round cover glasses with a diameter of 22 mm were used. The solution was poured on each cover glass in a final volume of 200 μL, containing 10 mM $CaCl_2$, and a total protein concentration of 50 μg mL^{-1}, including labeled Stm-l/AF488 with a concentration of 2 nM, the unlabeled Stm-l with a concentration of 50 μg mL^{-1} (for the negative control), or 100 nM AF488 (for the control experiment). Crystals were grown for 2, 4, 6, 8, 10, 12, 16, 20, 24, 36, or 48 h. For HRPXRD, circular cover glasses with a diameter of 32 mm were used. The solution in a final volume of 1 mL, containing 10 mM $CaCl_2$ and Stm-l at a total concentration of 5 or 50 μg mL^{-1}, and without Stm-l (control experiment contains 10% buffer A), was poured on each cover glass. The time of growth was 48 h. For each crystallization experiment, solid ammonium hydrocarbonate (2 g) was used in a closed desiccator. After incubation at room temperature, the crystallization solution was removed and crystals were washed two times with milli-Q water and finally air-dried at room temperature. For ex situ heating experiments, samples were heated at 250 °C in an oven for 2 h.

Two-photon fluorescence microscopy (TPM)

Fluorescence was excited at $\lambda = 800$ nm with a Ti:sapphire laser (Chameleon, Coherent, Santa Clara, CA, USA). The laser beam was focused tightly by using a high numerical aperture oil-immersion microscope objective (100×, NA = 1.4). The sample was mounted on an XYZ piezoelectric scanning stage (Tritor, Piezosystem Jena GmbH, Jena, Germany), and the two-photon excited emission was collected in epi-fluorescence mode through the same microscope objective. The crystals were scanned at several *z* positions and 3D images were obtained.

Confocal laser scanning microscopy (CLSM)

Images of fluorescently labeled Stm-l/AF488 protein were acquired by using the Leica TCS SP5 II confocal system (Wetzlar, Germany) equipped with a 63×Oil (NA: 1.4) objective lens. Crystals were covered by immersion oil (type F, refractive index 1.518) before measurement. The fluorescence of Stm-l/AF488 was excited with $\lambda =$ 488 nm light (Ar ion laser at 31% of maximum power with 20% AOBS) and detected in the 520–785 nm range. Images were acquired by using LAS AF software version 2.2.1 and processed by using ImageJ version 1.48[52] or Icy platform version 1.9.5.0 software.[53]

High-resolution X-ray powder diffraction (HRPXRD)

HRPXRD analysis was carried out on the ID22 beamline of the European Synchrotron Radiation Facility (ESRF), Grenoble, France, that used a highly collimated and monochromatic beam to perform powder diffraction in the transmission setting. Powder samples were investigated at a wavelength of 0.41065 Å. Instrument calibration and wavelength refinement were performed with silicon standard NIST 640c. All samples were measured in a borosilicate 1 mm capillary. Fullprof software[54] was used for structure refinements with the Pseudo-Voigt peak shape functions. The refined model was based on 16 structural parameters and 12 instrumental and background parameters. Crystallite size and microstrain fluctuations were calculated as reported in the literature,[30,42] and strain information was expressed as $\Delta d/d_{rf}$ (d is the lattice parameter measured and d_{rf} the reference used for comparison).

Micro-Raman spectroscopy

Raman spectra in the 100–1500 cm^{-1} range were measured by using a Renishaw InVia Raman spectrometer (Wotton-under-Edge, UK) equipped with a confocal DM 2500 Leica optical microscope, a thermoelectrically cooled charge-coupled device (CCD) as a detector and a diode laser operating at $\lambda = 830$ nm. The spectral resolution was set to 1 cm^{-1}. Each spectral profile is an average of five spectra.

Scanning electron microscopy (SEM)

Structural characterization of the calcium carbonate crystals was achieved through SEM by using a Philips XL-20 scanning microscope (Amsterdam, Netherlands) at an accelerating voltage of 25.0 kV. Each cover glass of the crystallization experiments had previously been coated with a carbon layer. Crystals were counted (covering most of the representative areas of 4.45 mm^2) and diameters were measured (50 crystals for each time) at different time points of the SEM images, by using the plugin ObjectJ 1.03w[55] of the free and open-source ImageJ 1.47v[56] image processing software.

Acknowledgements

We are indebted to the ESRF from Grenoble in France for the use of their powder high-resolution beamline ID22. This work was supported by National Science Centre grant (UMO-2015/19/B/ST10/02148) and by a statutory activity subsidy from the Polish Ministry of Science and Higher Education for the Faculty of Chemistry of Wroclaw University of Science and Technology.

Conflict of interest

The authors declare no conflict of interest.

Keywords: biominerals · calcium · crystal growth · proteins · X-ray diffraction

[1] L. Addadi, S. Weiner, M. Geva, *Z. Kardiol.* **2001**, *90*, III92 – 98.
[2] A. L. Boskey, *Connect. Tissue Res.* **2003**, *44*, 5 – 9 *Suppl 1*.
[3] Q. Feng, *Prog. Mol. Subcell. Biol.* **2011**, *52*, 141 – 197.
[4] A. L. Boskey, E. Villarreal-Ramirez, *Matrix Biol.* **2016**, *52 – 54*, 43 – 59.
[5] A. George, A. Veis, *Chem. Rev.* **2008**, *108*, 4670 – 4693.
[6] M. Wojtas, P. Dobryszycki, A. Ożyhar, O. Andrzej, in *Advanced Topics in Biomineralization* (Ed.: J. Seto), InTech, Croatia, **2012**, pp. 3 – 32
[7] F. Marin, G. Luquet, in *Handbook of Biomineralization* (Eds.: E. Bäuerlein, P. Behrens, M. Epple), Wiley-VCH, Weinheim, **2007**, pp. 273 – 290.
[8] S. Cruz, J. C. Shiao, B. K. Liao, C. J. Huang, P. P. Hwang, *J. Exp. Biol.* **2009**, *212*, 639 – 647.
[9] P. J. Kozel, R. A. Friedman, L. C. Erway, E. N. Yamoah, L. H. Liu, T. Riddle, J. J. Duffy, T. Doetschman, M. L. Miller, E. Lou Cardell, G. E. Shull, *J. Biol. Chem.* **1998**, 18693 – 18696.
[10] S. Weiner, P. M. Dove, *Rev. Miner. Geochem.* **2003**, *54*, 1 – 29.
[11] S. Younis, Y. Kauffmann, L. Bloch, E. Zolotoyabko, *Cryst. Growth Des.* **2012**, *12*, 4574 – 4579.
[12] L. Addadi, D. Joester, F. Nudelman, S. Weiner, *Chem. Eur. J.* **2006**, *12*, 980 – 987.
[13] A. Williams, M. Cusack, *J. Struct. Biol.* **1999**, *126*, 227 – 240.
[14] F. H. Wilt, *J. Struct. Biol.* **1999**, *126*, 216 – 226.
[15] Y. W. Lundberg, Y. Xu, K. D. Thiessen, K. L. Kramer, *Dev. Dyn.* **2015**, *244*, 239 – 253.
[16] C. Söllner, H. Schwarz, R. Geisler, T. Nicolson, *Dev. Genes Evol.* **2004**, *214*, 582 – 590.
[17] A. L. Boskey, *Elements* **2007**, *3*, 385 – 391.
[18] A. N. Popper, R. R. Fay, C. Platt, O. Sand, in *Sensory Processing in Aquatic Environment* (Eds.: S. P. Collin, N. J. Marshall), Springer, New York, **2003**, pp. 3 – 38.
[19] A. N. Popper, J. Ramcharitar, S. E. Campana, *Mar. Freshwater Res.* **2005**, *56*, 497 – 504.
[20] G. Borelli, M. E. Guibbolini, N. Mayer-Gostan, F. Priouzeau, H. De Pontual, D. Allemand, S. Puverel, E. Tambutte, P. Payan, *J. Exp. Biol.* **2003**, *206*, 2685 – 2692.
[21] M. Guibbolini, G. Borelli, N. Mayer-Gostan, F. Priouzeau, H. De Pontual, D. Allemand, P. Payan, *Comp. Biochem. Physiol. A Mol. Integr. Physiol.* **2006**, *145*, 99 – 107.
[22] A. Jolivet, J. F. Bardeau, R. Fablet, Y. M. Paulet, H. de Pontual, *Anal. Bioanal. Chem.* **2008**, *392*, 551 – 560.
[23] C. Söllner, M. Burghammer, E. Busch-Nentwich, J. Berger, H. Schwarz, C. Riekel, T. Nicolson, *Science* **2003**, *302*, 282 – 286.
[24] Y. J. Kang, A. K. Stevenson, P. M. Yau, R. Kollmar, *J. Assoc. Res. Otolaryngol.* **2008**, *9*, 436 – 451.
[25] F. Marin, B. Pokroy, G. Luquet, P. Layrolle, K. De Groot, *Biomaterials* **2007**, *28*, 2368 – 2377.
[26] B. Bajoghli, M. Ramialison, N. Aghaallaei, T. Czerny, J. Wittbrodt, *Dev. Dyn.* **2009**, *238*, 2860 – 2866.
[27] M. Kalka, N. Markiewicz, M. Ptak, E. D. Sone, A. Ożyhar, P. Dobryszycki, M. Wojtas, *FASEB J.* **2019**, *33*, 6877 – 6886.
[28] M. Różycka, M. Wojtas, M. Jakób, C. Stigloher, M. Grzeszkowiak, M. Mazur, A. Ożyhar, *PLoS One* **2014**, *9*, e114308.
[29] B. Pokroy, A. N. Fitch, F. Marin, M. Kapon, N. Adir, E. Zolotoyabko, *J. Struct. Biol.* **2006**, *155*, 96 – 103.
[30] E. Weber, L. Bloch, C. Guth, A. N. Fitch, I. M. Weiss, B. Pokroy, *Chem. Mater.* **2014**, *26*, 4925 – 4932.
[31] G. Caglioti, A. Paoletti, F. P. Ricci, *Nucl. Instrum.* **1958**, *3*, 223 – 228.
[32] P. Scherrer, in *Kolloidchemie: Ein Lehrbuch* (Ed.: R. Zsigmondy), Springer, Heidelberg, **1912**, pp. 387 – 409.
[33] R. K. Benninger, D. W. Piston, *Curr. Protoc. Cell Biol.* **2013**, *59*, 4.11.1.
[34] S. Weiner, L. Addadi, *J. Mater. Chem.* **1997**, *7*, 689 – 702.
[35] E. Zolotoyabko, *Adv. Mater. Interfaces* **2017**, *4*, 1600189.
[36] S. Kamat, X. Su, R. Ballarini, A. H. Heuer, *Nature* **2000**, *405*, 1036 – 1040.
[37] B. Pokroy, A. N. Fitch, E. Zolotoyabko, *Cryst. Growth Des.* **2007**, *7*, 1580 – 1583.
[38] K. Gries, R. Kröger, C. Kübel, M. Fritz, A. Rosenauer, *Acta Biomater.* **2009**, *5*, 3038 – 3044.
[39] I. Polishchuk, A. A. Bracha, L. Bloch, D. Levy, S. Kozachkevich, Y. Etinger-Geller, Y. Kauffmann, M. Burghammer, C. Giacobbe, J. Villanova, G. Hendler, C.-Y. Sun, A. J. Giuffre, M. A. Marcus, L. Kundanati, P. Zaslansky, N. M. Pugno, P. U. P. A. Gilbert, A. Katsman, B. Pokroy, *Science* **2017**, *358*, 1294 – 1298.
[40] S. Borukhin, L. Bloch, T. Radlauer, A. H. Hill, A. N. Fitch, B. Pokroy, *Adv. Funct. Mater.* **2012**, *22*, 4216 – 4224.
[41] B. Pokroy, A. Fitch, E. Zolotoyabko, *Adv. Mater.* **2006**, *18*, 2363 – 2368.
[42] Y. Y. Kim, A. S. Schenk, J. Ihli, A. N. Kulak, N. B. Hetherington, C. C. Tang, W. W. Schmahl, E. Griesshaber, G. Hyett, F. C. Meldrum, *Nat. Commun.* **2014**, *5*, 4341.
[43] M. A. Hood, H. Leemreize, A. Scheffel, D. Faivre, *Biomineralization* **2016**, *196*, 147 – 154.
[44] V. N. Uversky, *Protein J.* **2009**, *28*, 305 – 325.
[45] E. Weber, C. Guth, I. M. Weiss, *PLoS One* **2012**, *7*, e46653.
[46] P. Bots, L. G. Benning, J. Rodriguez-Blanco, T. Roncal-Herrero, S. Shaw, *Cryst. Growth Des.* **2012**, *12*, 3806 – 3814.
[47] L. N. Schultz, K. Dideriksen, L. Lakshtanov, S. S. Hakim, D. Müter, F. Haußer, K. Bechgaard, S. L. S. Stipp, *Cryst. Growth Des.* **2014**, *14*, 552 – 558.
[48] D. Gebauer, A. Völkel, H. Cölfen, A. Volkel, H. Colfen, *Science* **2008**, *322*, 1819 – 1822.
[49] D. Gebauer, *Mineralis* **2018**, *8*, 179.
[50] M. D. Sikirić, H. Füredi-Milhofer, *Adv. Colloid Interface Sci.* **2006**, *128 – 130*, 135 – 158.
[51] D. E. Kile, D. D. Eberl, A. R. Hoch, M. M. Reddy, *Geochim. Cosmochim. Acta* **2000**, *64*, 2937 – 2950.
[52] C. A. Schneider, W. S. Rasband, K. W. Eliceiri, *Nat. Methods* **2012**, *9*, 671.

[53] F. de Chaumont, S. Dallongeville, N. Chenouard, N. Herve, S. Pop, T. Provoost, V. Meas-Yedid, P. Pankajakshan, T. Lecomte, Y. Le Montagner, T. Lagache, A. Dufour, J. C. Olivo-Marin, *Nat. Methods* **2012**, *9*, 690 – 696.
[54] J. Rodríguez-Carvajal, *Phys. B* **1993**, *192*, 55 – 69.
[55] N. O. E. Vischer, P. G. Huls, C. L. Woldringh, *Binary* **1994**, *6*, 160 – 166.
[56] M. D. Abràmoff, P. J. Magalhães, S. J. Ram, *Biophoton. Int.* **2004**, *11*, 36 – 42.
[57] W. Kaminsky, *J. Appl. Crystallogr.* **2007**, *40*, 382 – 385.

Manuscript received: May 10, 2019
Accepted manuscript online: June 26, 2019
Version of record online: August 12, 2019

